Additive Manufacturing 92 (2024) 104403

Contents lists available at ScienceDirect

Additive Manufacturing

journal homepage: www.elsevier.com/locate/addma

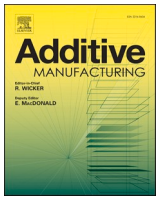

Full Length Article

A mechanism-based optimization strategy with adaptive laser power for laser powder bed fusion

Tao Yu, Shiwei Zhao, Jidong Zhao *

Hong Kong University of Science and Technology, Clearwater Bay, Kowloon, Hong Kong, China

ARTICLE INFO

Keywords:
Keyhole fluctuation
Optimization
Adaptive laser power
Laser powder bed fusion

ABSTRACT

The presence of keyhole-induced porosity significantly limits the application of laser powder bed fusion (L-PBF) in the additive manufacturing industry. Typically, a trial-and-error approach is used to select the best printing strategies for material type, powder bed, and laser beam to optimize the manufacturing process. This paper proposes an optimization strategy that uses adaptive laser power based on key understanding of the physical mechanisms of keyhole fluctuations. We identify and analyze five stages of the keyhole pore formation process, including the "J"-like keyhole formation, keyhole closure, keyhole pore collapse, keyhole pore splitting, and keyhole pore motion. Our simulation results suggest that reducing the laser power at the onset of "J"-like keyhole formation is an appropriate optimization approach. We propose adaptive indices to quantify keyhole fluctuations and predict the onset of "J"-like keyhole formation, which facilitates the use of adaptive laser power for optimization. Two parametric studies are conducted to investigate the impact of the optimization criterion and laser power adjustment on keyhole instability. The results demonstrates that our optimization strategy can effectively stabilize the keyhole and reduce the occurrence of keyhole porosity.

1. Introduction

Laser powder bed fusion (L-PBF) is a process to create a three-dimensional (3D) object by selectively melting a flat powder bed layer by layer with a laser beam. Despite its prevailing application, a significant defect may arise due to keyhole-induced porosity during the melting process [1–4]. Previous experimental studies have focused on investigating the impact of various controlling parameters on the printing outcomes, including laser scanning speed, layer thickness, laser beam incident angle [5], ambient pressure [6], and energy density [7,8] (see a summary in Table 1). For instance, a boundary for keyhole porosity in the laser power-velocity space can be identified by repeating the manufacturing process with different laser powers and scanning velocities, offering a guideline for selecting an appropriate laser strategy [1]. Indeed, experimental studies have provided valuable insights into the understanding and optimization of practical printing procedures for quality control of manufactured parts. However, experimental approaches often select fixed parameter values for the entire printing process through costly trial and error. The selected parameters are often too conservative for avoiding the occurrence of inherent defects, especially porosity, which hinders the improvement of manufacturing efficiency [1].

Optimization approaches have been applied to improve the production rate and mechanical properties of fabricated parts. For example, two adaptive laser power strategies [9,10] have recently been proposed to address keyhole-induced porosity at the start and turn points of the laser scanning path. Analytical approaches, such as using normalized enthalpy [9] and the Weber number [10], are employed to analyze the optimization strategy to reduce keyhole instability. However, previous studies have partial or even no consideration to the influence of significant keyhole fluctuations, such as perturbative and intrinsic oscillations [11], that commonly occur during typical melting processes [1]. This is because accurately predicting the formation of keyhole pores remains challenging for the implementing adaptive laser power throughout the entire scanning path.

In this study, we propose a mechanism-based optimization strategy to stabilize the keyhole and reduce the keyhole porosity using a high-fidelity, physics-based computational approach. The proposed approach has three innovative features: (1) it enables us to uncover the underlying physical mechanisms that govern the two oscillation modes of a keyhole throughout the entire scanning path. (2) It introduces an adaptive parameter to quantify keyhole dynamics and predict keyhole

* Corresponding author.
E-mail address: jzhao@ust.hk (J. Zhao).

https://doi.org/10.1016/j.addma.2024.104403
Received 24 March 2024; Received in revised form 30 July 2024; Accepted 30 August 2024
Available online 31 August 2024

Table 1
Typical experimental studies of laser powder bed fusion.

Variables	Typical specific factors	
Powder layer	Grain Size Distribution [12,13]	Powder layer thickness [14,15]
	Radius ratio of laser and powder [13]	Preheating temperature [16]
Laser beam	Laser energy density [13,17,18]	Energy distribution [19–21]
	Hatch distance [7,22–24]	Scanning strategy [25–28]
Material type	Printing materials (Aluminum, stainless steel, Ti−6Al−4 V, inconel) [29,30]	

pore formation. (3) It establishes an adaptive laser power strategy that helps to reduce the formation of keyhole pores without compromising printing efficiency.

2. Methodology and model setup

2.1. Methodology

This work employs our recently developed computational framework, which includes key components of a multiphase model, phase transition model, laser absorption model, and multi-physics governing equations as described in our previous work [31]. The framework has been thoroughly validated using various metrics, including the morphology of melt track, laser absorption, the shape of keyhole, the formation of keyhole pores, phase transitions, and powder motion [31–33]. The numerical method is briefly described here to complete the presentation.

2.2. Multi-phase model of the melting process

The proposed computational framework is based on fully resolved Computational Fluid Dynamics (CFD) and Discrete Element Method (DEM) to model the melting process of L-PBF [33]. During the melting process, there are co-existing multiple phases, including the solid metal, melt flow, metallic vapor, and ambient gas. Given the focus of this study on the thermo-mechanical dynamics of the keyhole and keyhole pore in a bare plate, it is reasonable to simplify the melting process as a solid-fluid two-phase problem [34]. Metal vapor and shielding gas are treated as one ambient gas [6,35,36] in the formation of the keyhole depression. Mass transfer, recoil pressure, and latent heat of the metallic vapor are taken into consideration in the modelling of the melting process. To facilitate numerical modeling [37], the solid or partially melted metal is modeled as a high-viscosity fluid with Darcy's effects [14,32,37,38].

The volume of fluid (VOF) method is utilized to solve the co-existing multiphase fluids based on their corresponding volume fractions, which include the solid metal, melt flow, and ambient gas. The volume fractions of the metal and gas are represented by α_1 and α_2, respectively, ranging from 0 to 1 and satisfying the condition $\alpha_1 + \alpha_2 = 1$. The equivalent properties of the multiphase system, including density (ρ), viscosity (μ), thermal conductivity (k), and heat capacity (C), are obtained as follows:

$$\begin{cases} \rho = \alpha_1\rho_1 + \alpha_2\rho_2 \\ \mu = \alpha_1\mu_1 + \alpha_2\mu_2 \\ k = \alpha_1 k_1 + \alpha_2 k_2 \\ C = \alpha_1\dfrac{\rho_1}{\rho}C_1 + \alpha_2\dfrac{\rho_2}{\rho}C_2 \end{cases}, \tag{1}$$

where the subscripts (1 and 2) denote the metal phase and the gas phase, respectively.

2.3. Multi-way phase transitions and laser absorption

Different phase transition processes may occur during the melting process of L-PBF, such as melting, solidification, evaporation, and condensation. The following describes the specific models adopted for these phase transition processes and the laser absorption model.

1. Melting and solidification

The melting and solidification processes are simplified by assuming a significant change in the viscosity of the metal fluid. The alteration of metal viscosity μ with temperature is described using the following expression [37]:

$$\ln\mu = \frac{1}{2}\mathrm{erfc}\left[\frac{4}{\ln T_\mathrm{l} - \ln T_\mathrm{s}} \bullet \left(\ln T - \frac{\ln(T_\mathrm{l}) + \ln(T_\mathrm{s})}{2}\right)\right] \bullet (\ln\mu_\mathrm{s} - \ln\mu_\mathrm{l}) + \ln\mu_\mathrm{l}, \tag{2}$$

where μ_s and μ_l are the viscosities at the solidus temperature T_s and liquidus temperature T_l, respectively. The term erfc () denotes the complementary Gaussian error function.

2. Evaporation

The mass loss rate ($\dot{m}_\mathrm{v}$), recoil pressure (P_re), and heat loss rate (Q_v) of the metal due to evaporation in the ambient atmosphere are calculated using a recently proposed evaporation model [39], i.e.,

$$\dot{m}_\mathrm{v} = -\left(1 - \frac{P_3}{P_\mathrm{e}}\sqrt{\frac{T}{T_3}}\beta F^-\right)P_\mathrm{e}\sqrt{\frac{M}{2\pi RT}}, \tag{3}$$

$$P_\mathrm{re} = \frac{\mathrm{e}^{D^2}}{2}\left(2D^2 + 1\right)\left(F^- + \sqrt{\frac{T_3}{T}}G^-\right)P_\mathrm{e}, \tag{4}$$

$$Q_\mathrm{v} = \dot{m}_1 L_\mathrm{v}, \tag{5}$$

where T is the temperature of the liquid surface; P_e is the saturated vapor pressure; P_3 and T_3 are the pressure and temperature out of the Knudsen layer [40], respectively; M is the molar mass and R is a universal gas constant; L_v is the latent heat of evaporation; D, F^- and G^- are dimensionless variables related to the ratio of isochoric and isobaric specific heat capacity of the gas and the Mach number out of the Knudsen layer [39].

3. Condensation

Badillo's condensation model [41–43] is utilized to calculate the rate of vapor condensation within a closed keyhole pore, i.e.,

$$\dot{m}_\mathrm{c} = \frac{6\sqrt{2}}{5}\frac{k_1(T - T_\mathrm{b})}{wL_\mathrm{v}}, \tag{6}$$

where k_1 is the heat conductivity of the metal, T_b is the boiling temperature, L_v is the latent heat of evaporation, and w is the characteristic length of the interface which is approximated by the size of the CFD cell [43].

4. Laser absorption model

The laser absorption model is built on our proposed VOF-compatible ray-tracing model [31,33]. This model features key considerations of the Fresnel reflection and refraction at the metal surface for the incident laser, laser attenuation and absorption in the metal during the scanning process, the impact of the metal state on the attenuation distance, and the influence of surface temperature on laser reflectivity. Detail of the laser absorption model and its numerical implementation can be referred to [31,33].

2.3.1. Governing equations of the multiphysics processes

1. Advection equation

Two interphase mass transfer rates, namely $\dot{m}_v$ and $\dot{m}_c$, are considered to represent the vaporization of liquidus metal into metallic vapor and the condensation of metallic vapor into liquidus metal, respectively. Both the metal and gas phases are assumed to be incompressible and are solved using the following advection equation:

$$\begin{cases} \dfrac{\partial \alpha_1}{dt} + \nabla \bullet (\alpha_1 \mathbf{u}) = \dfrac{2\alpha_1 \dot{m}_v - 2\alpha_2 \dot{m}_c}{\rho_1} |\nabla \alpha_1| \\ \alpha_2 = 1 - \alpha_1 \end{cases}, \tag{7}$$

where $\mathbf{u}$ is the velocity; α_1 and α_2 represent the volume fractions of the metal and the gas, respectively; $|\nabla \alpha_1|$ is an interface term to transform a surface term per unit area into a volumetric term [44–46]; α_1 or α_2 is a sharp surface term to smear out the interphase [47].

2. Momentum equation

Based on the Navier-Stokes equation, the following momentum equation is introduced to consider various physical phenomena, including the surface tension, Darcy's effects, recoil pressure, and Marangoni's flow, as shown in the RHS of the following equation.

$$\begin{aligned} \frac{\partial}{\partial t}(\rho \mathbf{u}) + \nabla \cdot (\rho \mathbf{u} \otimes \mathbf{u}) \quad &= -\nabla p + \nabla \cdot (\mu \cdot (\nabla \mathbf{u})) + c\sigma |\nabla \alpha_1| \frac{2\rho}{\rho_1 + \rho_2} \mathbf{n} \\ &- K_c \frac{(\alpha_1 - \alpha_m)^2}{\alpha_m^3 + C_k} \mathbf{u} + P_{re} |\nabla \alpha_1| \frac{2\rho}{\rho_1 + \rho_2} \mathbf{n} \\ &+ \frac{d\sigma}{dT} (\nabla T - \mathbf{n}(\mathbf{n} \cdot \nabla T)) |\nabla \alpha_1| \frac{2\rho}{\rho_1 + \rho_2} \end{aligned}, \tag{8}$$

where p is the pressure given by $p = p_d + \rho g h$; p_d is the dynamic pressure; g is the gravitational acceleration, and h is the reference height [37]; K_c is the permeability coefficient; C_k is a small constant to avoid division by zero; α_m is the volume fraction of the molten metal which can be approximated using a Gaussian error function [37]; C is the curvature of the metal-gas interface, and $c = -\nabla \bullet \mathbf{n}$. $\mathbf{n}$ is the unit normal vector at the interface, and $\mathbf{n} = \nabla \alpha_1 / |\nabla \alpha_1|$; $2\rho/(\rho_1 + \rho_2)$ is a sharp surface force term to smear out the interphase [44,47]; T_s is the solidus temperature; $d\sigma/dT$ represents the change of surface tension coefficient σ with respect to temperature. The volume fraction of the molten metal α_m and the surface tension coefficient σ [37] can be written as:

$$\alpha_m = \frac{\alpha_1}{2} \left[1 + \mathrm{erf}\left(4 \Big/ (T_l - T_s) \left(T - \frac{T_l + T_s}{2} \right) \right) \right], \tag{9}$$

$$\sigma = \begin{cases} \dfrac{\sigma_l}{1 + \mathrm{erf}2} \left[1 + \mathrm{erf}\left(\dfrac{4}{T_l - T_s} \left(T - \dfrac{T_l + T_s}{2} \right) \right) \right] & T \le T_l \\ \sigma_l + \dfrac{\partial \sigma}{\partial T} T & T > T_l \end{cases}, \tag{10}$$

where σ_l is the surface tension coefficient of the metal at the liquidus temperature.

(3) Temperature equation

The following temperature equation derived from the energy conservation is solved to update the thermal field, which includes multiple heat transfers due to laser heat, conduction, dissipation, fusion, convection, radiation, and vaporization [37], respectively,

$$\begin{aligned} \frac{\partial (C\rho T)}{\partial t} + \nabla (C\rho T) \cdot \mathbf{u} &= S_l + \nabla \cdot (k \nabla T) + \mu (\nabla \mathbf{u} + \mathbf{u} \nabla) : \nabla \mathbf{u} \\ &- L_f \left[\frac{\partial}{\partial t} (\rho \alpha_m) + \nabla \cdot (\rho \mathbf{u} \alpha_m) \right] - h_c (T - T_{ref}) |\nabla \alpha_1'| \frac{2C\rho}{C_1 \rho_1 + C_2 \rho_2} \\ &- \sigma_{sb} \left(T^4 - T_{ref}^4 \right) |\nabla \alpha_1'| \frac{2C\rho}{C_1 \rho_1 + C_2 \rho_2} - Q_v |\nabla \alpha_1'| \frac{2C\rho}{C_1 \rho_1 + C_2 \rho_2} \end{aligned}, \tag{11}$$

where L_f is the latent heat of fusion; h_c is the convective heat transfer coefficient; T_{ref} is the reference temperature, and σ_{sb} is the Stefan-Boltzmann constant; S_l is the laser input obtained from our previous VOF compatible ray-tracing model [33] with a modified reflectivity and absorption coefficient described in the laser absorption model.

2.4. Model setup and parameter selection

To study the effect of laser optimization strategy on the keyhole instability, this study focuses on the melting process of a bare Ti-6Al-4 V plate subject to a single track of laser. The plate measures 864×448×368 μm, as shown in Fig. 1, and is larger than the simulation domain in our previous work [31] to capture longer keyhole evolutions during the laser melting process. The laser has a spot size of 100 μm with a power of 225 W, moving along the longest dimension direction (864 μm). Two scanning velocities of 50 cm/s and 45 cm/s are chosen to study the impact of laser intensity on keyhole fluctuation. The selection of these specific scanning velocities is based on a keyhole porosity boundary experimentally identified from [1] at different combinations of laser power and scan speed. By maintaining a suitable difference in scanning velocity, specifically 5 cm/s in this study, it becomes more feasible to quantitatively elucidate the impact of the proposed optimization strategy. The configuration of adaptive meshing and boundary conditions are set as identical to those used in our previous work [31], including a coarser mesh with a grid size of 16 μm and a finer mesh with a grid size of 4 μm. The time step is 1×10^{-7} s. The physical parameters and temperature-dependent thermal parameters used in the subsequent simulations are summarized in Appendix A.

3. Mechanism-based optimization strategy

According to previous optimization approaches proposed in the literature [5,6,48,49], a typical optimization strategy includes three steps: (i) selection of the stage at which laser optimization will be conducted, such as the rotation of keyhole, the expansion of keyhole, and

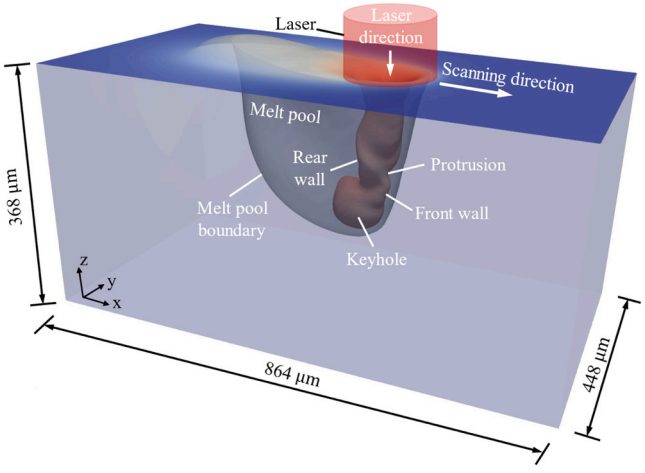

Fig. 1. Model setup of laser melting of a bare Ti-6Al-4 V plate, showing the entire simulation domain, the laser and scanning directions, the melt pool, the keyhole, and rear and front walls of the keyhole.

formation of "J"-like keyhole; (ii) introducing an index to quantitatively describe keyhole evolution and differentiate different keyhole characteristics; and (iii) establishing a criterion to determine the need for laser optimization and developing an optimization strategy, such as adjusting laser power, scanning velocity, and scanning path.

3.1. Selection of optimization stages

3.1.1. Five stages during a pore-formation process

According to both existing experimental observations and our simulation results, the entire process of pore formation can be classified into five stages: "J"-like keyhole formation (Stage I), keyhole closure (Stage II), keyhole pore collapse (Stage III), keyhole pore splitting (Stage IV), and keyhole pore motion (Stage V), as shown in Fig. 2. Experimental observations show that the duration of Stages III and IV is only around several microseconds [1], too short to make it possible for implementing optimization approaches to avoid pore formation. Once a keyhole pore is formed, its motion is dominantly influenced by the vortex in the melt pool, which varies with the position of the pore and keyhole fluctuations. This complex situation makes process optimization difficult. However, it is more efficient to avoid pore formation by implementing optimization strategies during early stages of the process, i.e., Stages I and II. Because of rather different thermo-mechanical dynamics in stages I and II, different optimization strategies are required, each with varying levels of stability and efficiency.

3.1.2. Thermo-mechanical dynamics in Stages I and II

Protrusions are important features in stages I and II, as previously reported [31]. They aid in the transfer of high-temperature fluid to the keyhole bottom, accelerate keyhole closure, and influence laser reflectivity. In this section, we discuss the typical process of keyhole pore formation, along with potential optimization approaches.

In Stage I, the protrusions move downward to the keyhole bottom, increasing the temperature at the bottom part and leading to the further expansion of the keyhole. The protrusions, which are propelled by the recoil pressure and are of high-speed and high-temperature, need to be controlled to improve keyhole stability. As shown in Fig. 3, reducing the laser power during Stage I is a practical approach to achieve this. Fig. 3 shows that decreasing the laser power results in a decrease in the protrusion velocity on the front keyhole wall and the keyhole bottom. Importantly, for the case with half laser power, no further keyhole expansion occurs, preventing further keyhole closure.

In Stage II, closure of the keyhole occurs when the protrusions of the side walls collide with each other. To prevent such keyhole closure, the motion of protrusions can be controlled. The protrusion on the rear keyhole wall is primarily influenced by the vortex flow in the melt pool, while the protrusion on the front keyhole wall is mainly controlled by the laser energy. Increasing the laser power can result in a higher velocity of the front protrusion, which increases the distance between the two protrusions, as depicted in Fig. 4B. One the other hand, increasing the laser power may cause a larger recoil pressure on the rear keyhole wall, which slows down the rear protrusion driven by the vortex in the melt pool. Specifically, at 5.5 μs, the velocity direction along the laser moving direction turns opposite to that at 0 μs, indicating a continuous separation of the two protrusions. Therefore, keyhole closure and keyhole pore formation can be effectively prevented by increasing the laser power.

It is important to note that protrusions are common occurrences during the manufacturing process. The objective of this study is to prevent the collision of two protrusions rather than eliminating the occurrence of protrusions, as demonstrated in Fig. 4. In the event of two protrusions approaching each other after 5.5 μs, the same laser strategy will be employed to avoid the occurrence of collision.

3.1.3. Relevance to optimization strategies

From the above observations, it is necessary and effective to adopt different laser optimization strategies according to the distinctive mechanisms of protrusions in stages I and II. Specifically, a lower laser power in Stage I restricts the motion of front protrusions and weakens the local rotation at the keyhole bottom, while a higher laser power in Stage II accelerates the motion of front protrusions and increases the distance between front and rear protrusions. However, increasing the laser power can make the keyhole and the powder bed unstable. It can increase the speed of the metallic vapor generated in the keyhole, which agitates the motion of surrounding powders and the spattering of metal pool fluid [33]. While increasing the recoil pressure helps separate the protrusions on the front and rear walls, it also amplifies the temperature gradient of the melt pool and increases the likelihood of new protrusions

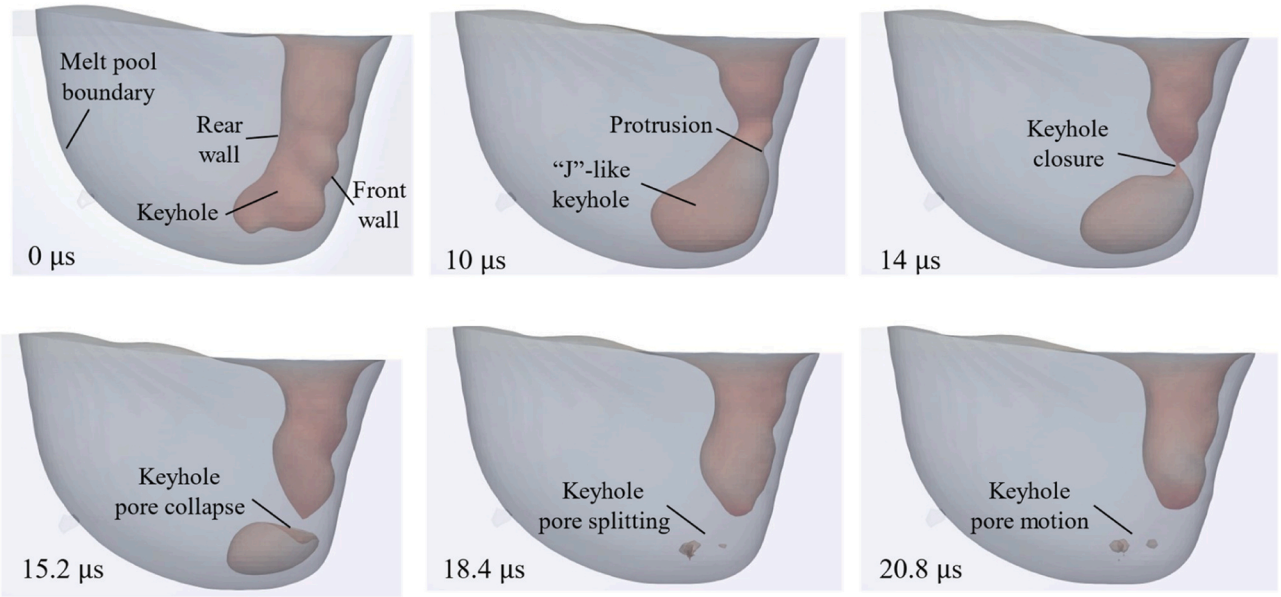

Fig. 2. One typical example of five stages during the complete process of pore formation based on our numerical simulations. Stage I is the "J"-like keyhole formation (0 μs – 10 μs). Stage II is the keyhole closure (10 μs – 14 μs). Stage III is the keyhole pore collapse (14 μs – 15.2 μs). Stage IV is the keyhole pore splitting (15.2 μs – 18.4 μs). Stage V is the keyhole pore motion (18.4 μs – 20.8 μs).

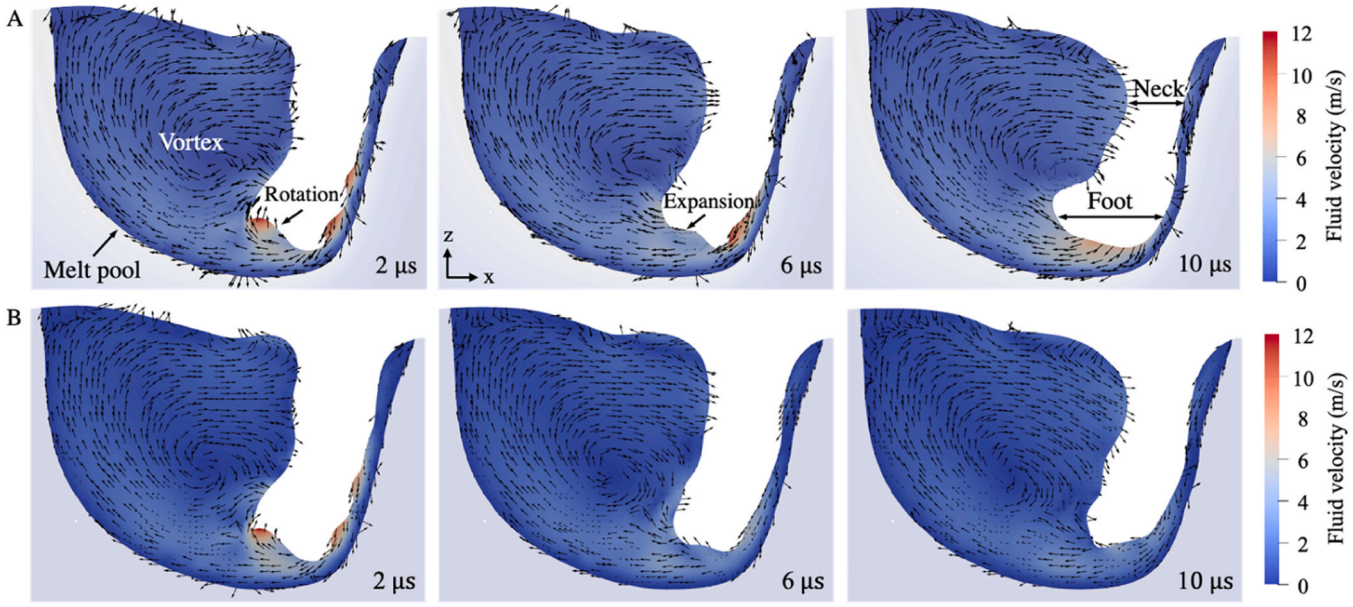

Fig. 3. Simulated velocity vector contours with an original laser power (A) and a half laser power (B).

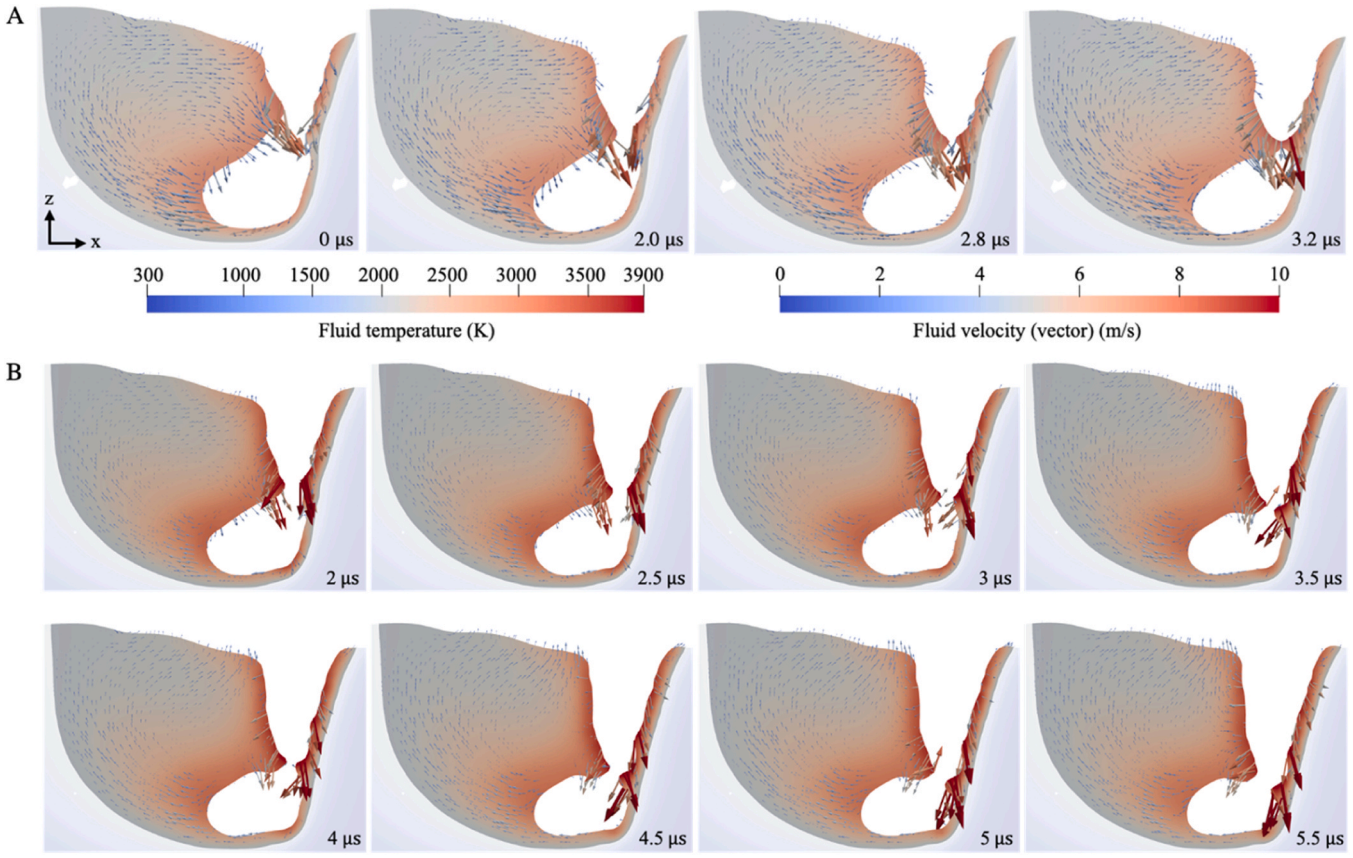

Fig. 4. Simulated velocity vector contours and temperature contours with an original laser power (A) and a double laser power (B).

forming on the front wall. Additionally, it can also raise more stringent requirements on the printing equipment. Therefore, decreasing the laser power in Stage I is a more preferred strategy than increasing the laser power in Stage II to improve keyhole stability and prevent keyhole pore formation.

3.2. Optimization indices

Section 3.1.2 describes a specific case with a simplified optimization approach, assuming prior knowledge when the stage begins. Nevertheless, the process of keyhole evolution is highly dynamic and characterized by irregular oscillations [11]. Previous studies have only focused on special time points, such as the starting and turning points of the

scanning path [48,49], instead of the entire scanning path. To predict various stages of keyhole pore formation, we need an index that provides a quantitative description of the complete keyhole evolution process. For example, the keyhole drilling speed or the collapse speed of keyhole walls [5,6,48,49] could serve as such an index. Based on this index, we could develop an optimization criterion to determine when laser optimization is necessary.

3.2.1. Keyhole oscillations

Keyhole oscillations exhibit two distinct modes: intrinsic and perturbative oscillations [11]. The mode of perturbative oscillation occurs exclusively under unstable keyhole conditions and plays a significant role in the formation of keyhole porosity. Previous studies have extensively described the mechanism of this oscillation mode [1,33]. Conversely, intrinsic oscillation can occur in both stable and unstable keyholes; however, it does not contribute significantly to keyhole porosity formation under unstable keyhole conditions. Although temporary keyhole pore may occur, the rapidly drilling keyhole can recapture and close the temporary pore [50,51]. Intrinsic oscillation arises due to the varying balance between Marangoni force, surface tension, and recoil pressure [11]. To quantify the keyhole oscillations more precisely, we classify keyholes into three types based on their distinct characteristics: stable “J”-like keyhole, shrinkage-induced keyhole pore, and expansion-induced keyhole pore. The stable "J"-like keyhole and shrinkage-induced keyhole pore correspond to the intrinsic mode of oscillation in stable and unstable keyholes, respectively. The expansion-induced keyhole pore corresponds to the perturbative mode of oscillation.

(1) Stable “J”-like keyhole

In Fig. 5, we can observe a typical life cycle of the stable “J”-like keyhole without any keyhole pore formation. The keyhole bottom expands during the formation process of the “J”-like keyhole from 402.5 μs to 410 μs and then gradually shrinks from 410 μs to 427.5 μs. The expansion is primarily due to the rising recoil pressure at the keyhole bottom, which is caused by the continuous incident laser, reflected laser from the front wall, and protrusions that transport high-temperature fluids from the front wall to the rear wall. The expansion process increases the surface area of the left keyhole tip (or “J” toe hereafter), causing the temperature to decrease. The decreasing recoil pressure and increasing surface tension at the “J” toe of the keyhole leads to further shrinkage of the keyhole bottom. As the keyhole shrinks, the temperature at the keyhole bottom increases again, initiating a new cycle of “J”-like keyhole formation (430 μs in Fig. 5). Further details regarding the mechanisms of the “J”-like keyhole formation process can be found in the literature [1,33].

(2) Expansion-induced keyhole pore

Fig. 6 illustrates a typical formation process of the keyhole pore caused by the expansion of the keyhole bottom. Like the stable "J"-like keyhole, the high temperature and large recoil pressure at the keyhole bottom significantly contribute to the expansion of the keyhole bottom and the formation of the "J"-like keyhole. However, compared to the stable "J"-like keyhole at 410 μs (shown in Fig. 5), a more extensive expansion of the keyhole bottom at 542.5 μs results in a shorter keyhole neck for the keyhole. Because of the shorter keyhole neck length, the possibility of collision between protrusions in the rear and front walls increases, as observed at 542.5 μs and 545 μs in Fig. 6. When two protrusions collide, they lead to the formation of a keyhole pore which can subsequently collapse, shrink, or break apart [1,33]. Further details regarding the mechanisms behind keyhole pore instability can be found in the literature [1,33], which has demonstrated that this type of keyhole pore is a significant factor in porosity formation.

(3) Shrinkage-induced keyhole pore

Fig. 7 depicts a typical shrinkage-induced keyhole pore formation process, in which a stable "J"-like keyhole occurs at 650 μs. As explained previously in the section “*Stable ‘J’-like keyhole*”, as the recoil pressure decreases and the surface tension increases at the “J” toe of the keyhole, the keyhole shrinks after the first "J"-like keyhole, resulting in a keyhole pore at 667.5 μs. During the shrinkage of the keyhole from 650 μs to 667.5 μs, the rear wall moves rapidly towards the front wall, with a maximum speed of 15 m/s observed at 661 μs, as shown in Fig. 8. Additionally, two vortices in the melt pool propel the fluids in two distinct zones (located at the left and bottom of the keyhole) towards the front wall, as observed in Fig. 8 from 661 μs to 666 μs. If the rising recoil pressure at the keyhole bottom is too small to counteract the motion of the rear wall, the two protrusions in the front and rear walls collide with each other, forming a keyhole pore; otherwise, a new cycle of "J"-like keyhole formation incepts.

Ultimately, the keyhole pore is captured by the rapidly drilling

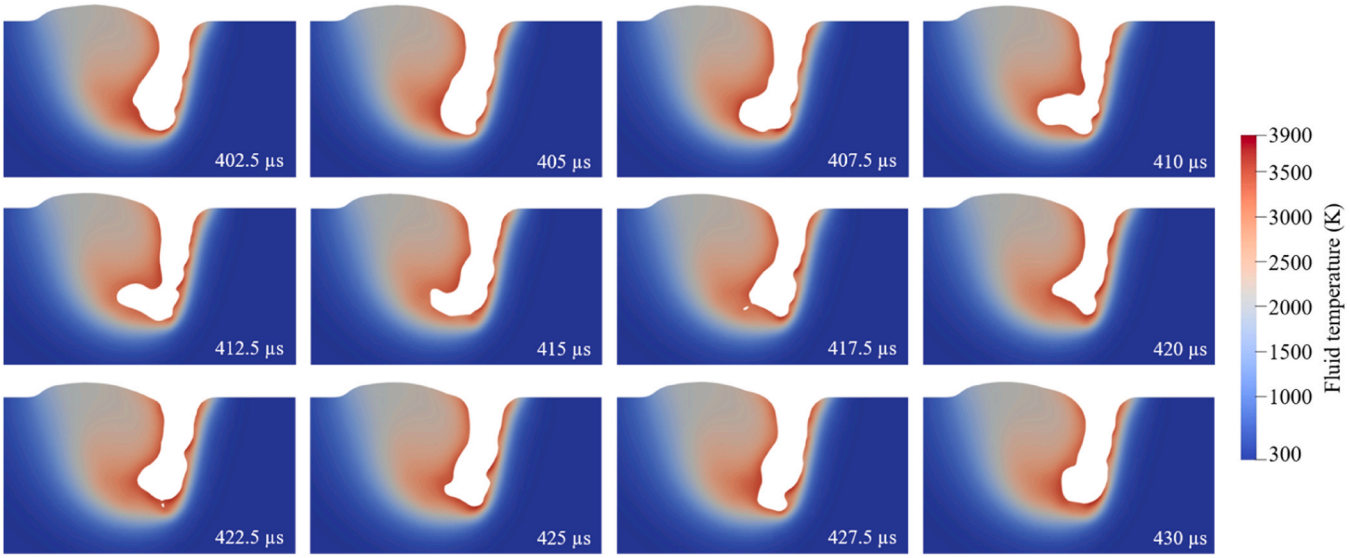

Fig. 5. Simulation results of the stable “J”-like keyhole with the temperature contour. Keyhole expansion occurs from 402.5 μs to 410 μs. Keyhole shrinkage occurs from 410 μs to 427.5 μs.

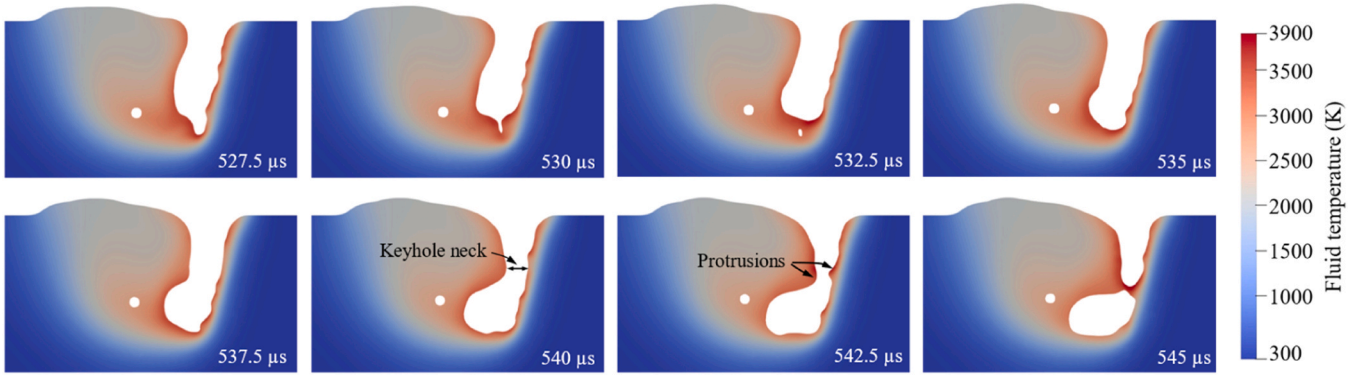

Fig. 6. Simulation results of the expansion-induced keyhole pore with the temperature contour.

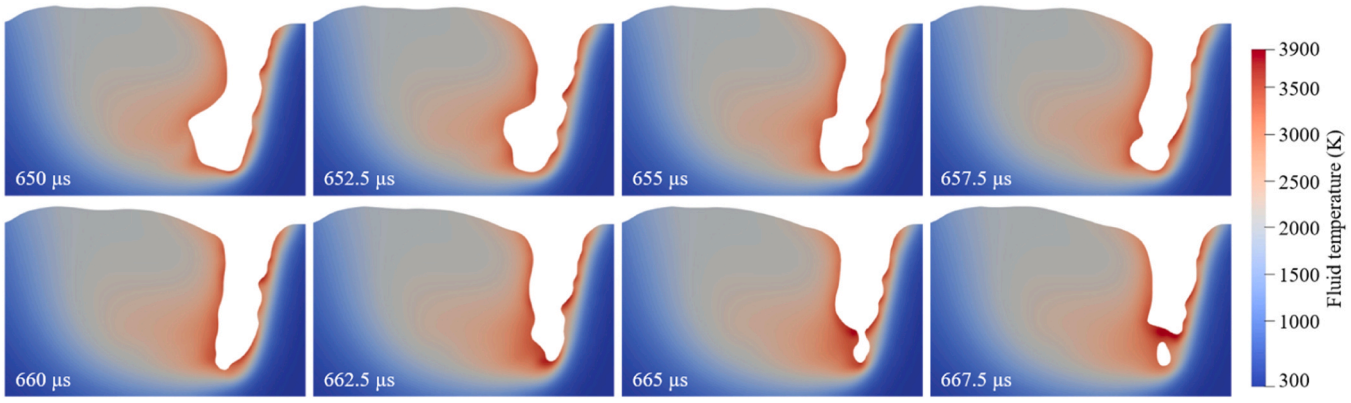

Fig. 7. Simulation results of the shrinkage-induced keyhole pore with the temperature contour.

keyhole and is not responsible for the keyhole porosity. Three reasons explain why the shrinkage-induced keyhole pore can be recaptured by the keyhole. Firstly, the shrinkage-induced keyhole pore is significantly smaller than the expansion-induced keyhole pore, resulting in a weak vapor condensation in the keyhole pore. For example, the volume of keyhole pore in Fig. 7 is only 2.5 % of that in Fig. 6. Only slight shrinkage of the keyhole pore, attributed to vapor condensation, is observed in Fig. 7 and Fig. 8. Thus, the shrinkage-induced pressure drop has only a moderate effect on the surrounding fluids. Secondly, while the recoil pressure at the keyhole bottom drives the surrounding liquids and keyhole pore downwards, a vortex in the keyhole bottom is generated by the shrinkage which lifts the keyhole pore upwards, as observed at 667 μs in Fig. 8. As the pore moves upward, fluids at the bottom right of the keyhole are propelled by the recoil pressure to further push the keyhole pore towards the keyhole, as observed at 670 μs in Fig. 8. Thirdly, keyhole shrinkage creates a keyhole pore at a specific position beneath the keyhole bottom that speeds up the collision between the rapidly drilling keyhole and the keyhole pore as the keyhole moving down. In contrast, the expansion-induced keyhole pore is located on the left side of the keyhole and is less likely to be recaptured by the rapidly drilling keyhole due to its location and the presence of significant vapor condensation in the keyhole pore [33,52].

3.2.2. *Quantification of keyhole fluctuations through three adaptive indices*

It is evident from preliminary simulation results in Section 3.1.2 and recent experimental observations [11] that the keyhole bottom undergoes significant deformation during the keyhole pore formation process, such as the expansion and shrinkage. The volume change of the keyhole bottom can be a suitable descriptor of keyhole fluctuations. However, in practice, only 2D images are available through advanced observation technologies, such as simultaneous high-speed synchrotron x-ray imaging (Fig. 9A), enabling the distinction between the gas phase and the metal phase based on distinct color representations. Subsequently, the gas region can be extracted from the X-ray image utilizing dynamic image recognition techniques. In this study, the adaptive indices are defined based on the change in gas area at the bottom of the keyhole within the 2D cross-section, satisfying $x < x_L$ and $z > z_n$ (as shown in Fig. 9), during a constant time interval of Δt. The variable x_L represents the x-coordinate of the laser center, and z_n represents the z-coordinate of the keyhole neck. The value of z_n varies for different cases, such as the scanning velocity, metal type, laser power, and other factors. To determine the z-coordinate of the keyhole neck, parametric studies using numerical simulations or experiments are necessary beforehand. For this study, the value of z_n is set to be 100 μm. The selected time interval must meet two requirements: (1) it should be sufficiently small to capture the key information of keyhole evolution; (2) it should be larger than the minimum time interval of megahertz x-ray images to allow adequate time for conducting optimization strategies. In this study, a time interval of 2.5 μs was used, which is approximately half the duration of a single "J"-like keyhole formation process and 2.7 times longer than the minimum time interval (0.92 μs) reported in the literature for megahertz x-ray images [1]. Notably, recent studies reported in [9] and [10] have explored the utilization of adjusted laser power at the microsecond timescale to enhance the efficiency and quality of the manufacturing process.

In this study, we propose three adaptive indices, namely the deformation index F_d, the absolute deformation index F_{ad}, and the expansion index F_e, to quantify the variation in the specific gas area at the bottom of the keyhole between two time intervals, as shown in Eqs. (12) to (14). These indices consider two parameters, the depth from the plate surface and the distance from the laser center, due to their significance in the melt flow at the keyhole bottom and far from the laser center, which are

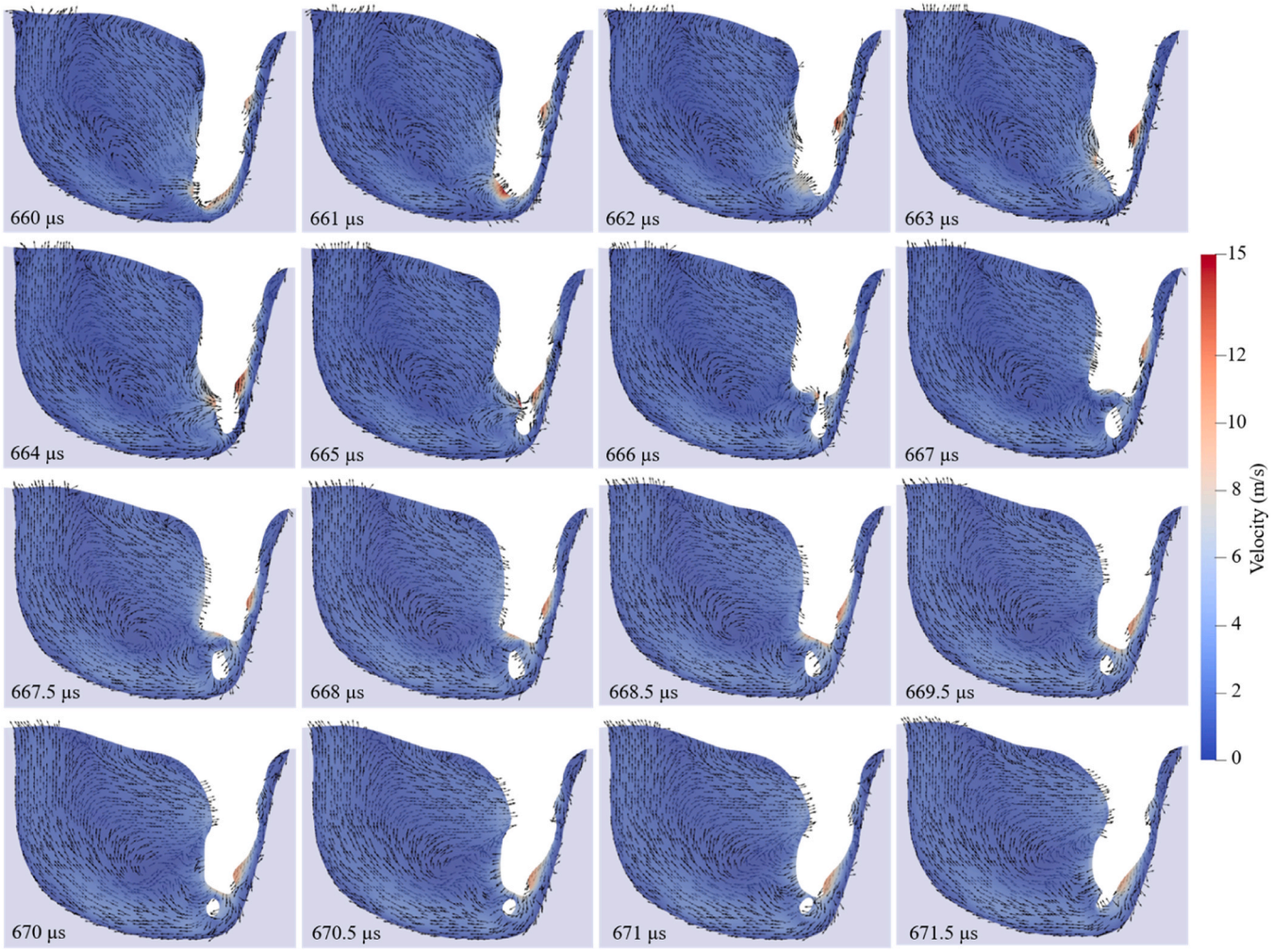

Fig. 8. Simulation results of the shrinkage-induced keyhole pore and the pore-recapture process with the velocity contour.

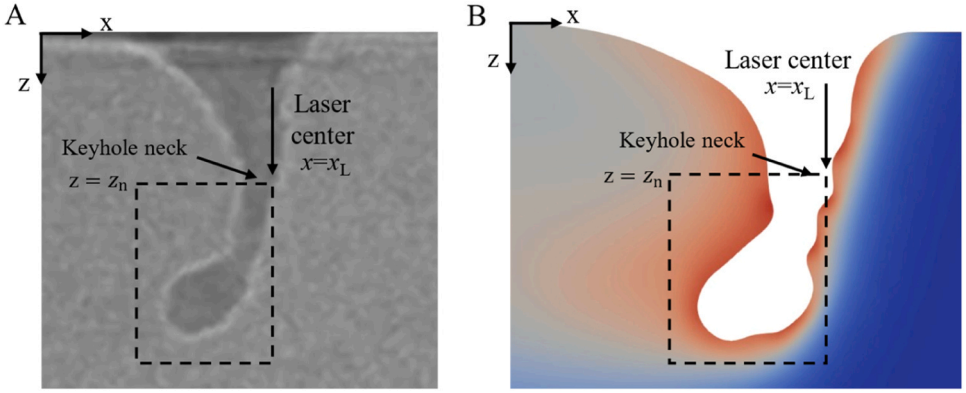

Fig. 9. Schematic diagram of the computational domain for the adaptive index in high-speed x-ray images [1] (A) and simulation results (B).

essential factors in the formation of the "J"-like keyhole. Specifically, the deformation index F_d and the absolute deformation index F_{ad} represent the change and the absolute change in the specific gas area at the keyhole bottom, respectively. The expansion index F_e is the sum of F_d and F_{ad}, representing the expansion of specific gas area at the keyhole bottom,

$$(F_d)^n = \sum_x \left(\sum_z (z \bullet \alpha_2)^n - \sum_z (z \bullet \alpha_2)^{n-1} \right) \frac{x - L_x}{\Delta L} \tag{12}$$

$$(F_{ad})^n = \sum_x \left| \sum_z (z \bullet \alpha_{gas})^n - \sum_z (z \bullet \alpha_{gas})^{n-1} \right| \frac{x - L_x}{\Delta L} \tag{13}$$

$$F_e = (F_d)^n + (F_{ad})^n \tag{14}$$

where α_2 is the volume fraction of gas; z is the z-coordinate calculated from the plate surface; L_x is the x-coordinate of the laser center; x is the x-coordinate of the keyhole bottom, satisfying $x < x_L$ and $z > z_n$, and ΔL

is the mesh size; $n-1$ and n denote the sequence of the time interval.

Fig. 10 presents the variation of the three indices along with formation processes of the stable “J”-like keyhole and keyhole pores during a typical melting process. In particular, Fig. 10 A shows that there is no clear correlation between the evolution of the keyhole and the indices of deformation and absolute deformation. Through the generation of the expansion index, multiple formation processes of the keyhole pore (due to keyhole expansion or shrinkage) and the stable "J"-like keyhole shown in Fig. 10B exhibit consistent characteristics, respectively. Fig. 11 illustrates a strong correlation between the variation of the expansion index and the fluctuations in the keyhole, demonstrating the reliability of the expansion index. Multiple distinct cycles of the keyhole volume change can be observed in Fig. 11, indicating the regular development of the keyhole expansion (i.e., “J”-like keyhole formation) and keyhole shrinkage, as shown in Fig. 5. Note that keyhole volume is a 3D parameter that cannot be directly obtained through existing 2D imaging observational technologies, whereas the expansion index F_e is a 2D parameter based on the central cross-section equivalent to the image obtained by simultaneous high-speed synchrotron x-ray imaging.

The expansion index F_e exhibits a sharp increase followed by a rapid decrease after reaching its local peak during one cycle of the stable "J"-like keyhole (shown as purple lines in Fig. 10). The surge increase of the expansion index corresponds to the expansion of the keyhole bottom, while the subsequent rapid decrease indicates the shrinkage of the keyhole, consistent with the phenomena of a stable “J”-like keyhole explained in the Section "*Keyhole oscillations*". During the cycle of the expansion-induced keyhole pore (red lines in Fig. 10), the change in F_e shares a similar trend to that observed during a cycle of the stable "J"-like keyhole. In contrast, during a cycle of the shrinkage-induced keyhole pore, F_e rapidly decreases due to the keyhole shrinkage, followed by a smaller fluctuation, indicating the generation and recapture of the keyhole pore.

Fig. 11 illustrates the temporal evolution of the keyhole volume, the expansion index, and three keyhole characteristics in two cases, each with a scanning velocity of 45 cm/s and 50 cm/s, respectively. The observed trend remains consistent between the two cases, indicating a similar behavior. However, the cycle period of keyhole expansion and shrinkage, as well as the frequency of the three keyhole characteristics, varies with the scanning velocity. It is important to note that a comprehensive investigation is needed to quantify these keyhole characteristics under different laser conditions in the future work, including the laser power and the scanning velocity. The current study serves as a preliminary work, proposing an optimization scheme aimed at stabilizing the keyhole and preventing the formation of keyhole pores.

3.3. Optimization scheme

3.3.1. Optimization criterion

Since the shrinkage-induced keyhole pore can be recaptured by the keyhole and will not contribute to the keyhole porosity, only the expansion-induced keyhole pore will be considered in our proposed optimization scheme. However, as numerically observed, it is

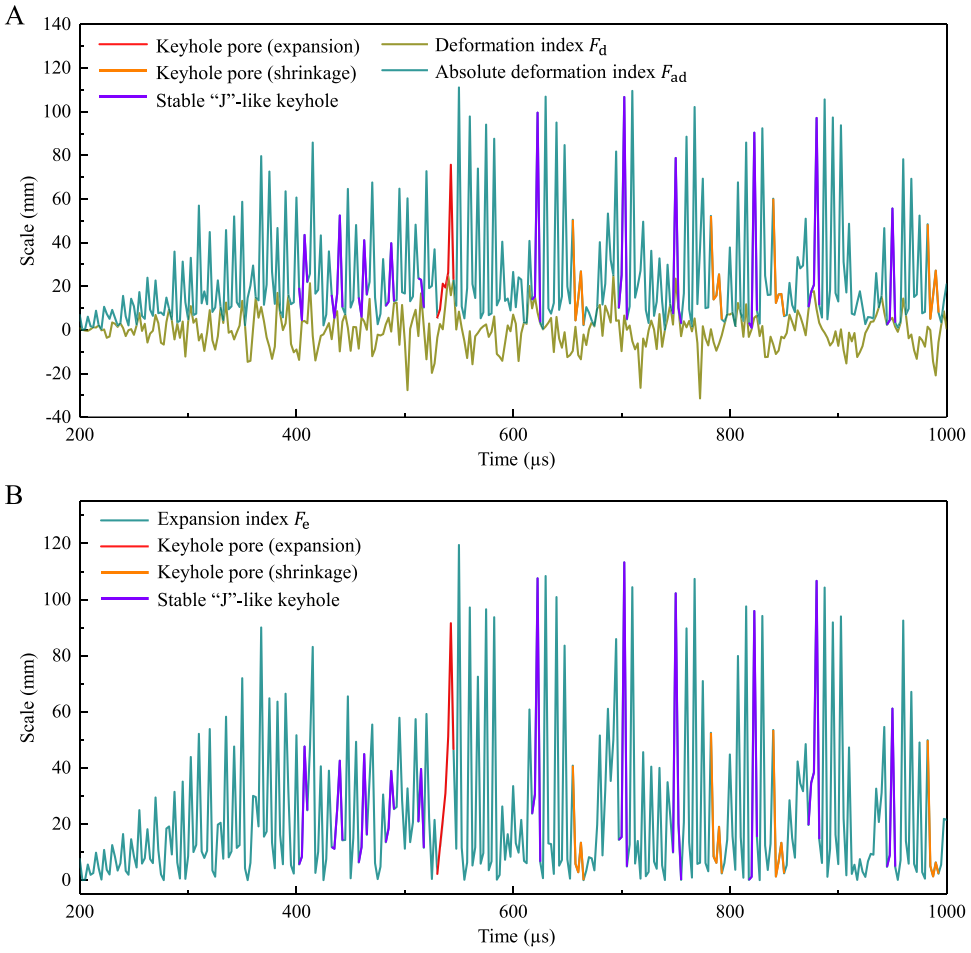

Fig. 10. (A) The evolution of the deformation index F_d and the absolute deformation index F_{ad} during the melting process. (B) The evolution of the expansion index F_e during the melting process. The time and corresponding indices for the formation processes of the expansion-induced keyhole pore, the shrinkage-induced keyhole pore, and the stable “J”-like keyhole occur are highlighted with red, orange, and purple lines, respectively. The laser power is 225 W and the scanning velocity is 50 cm/s.

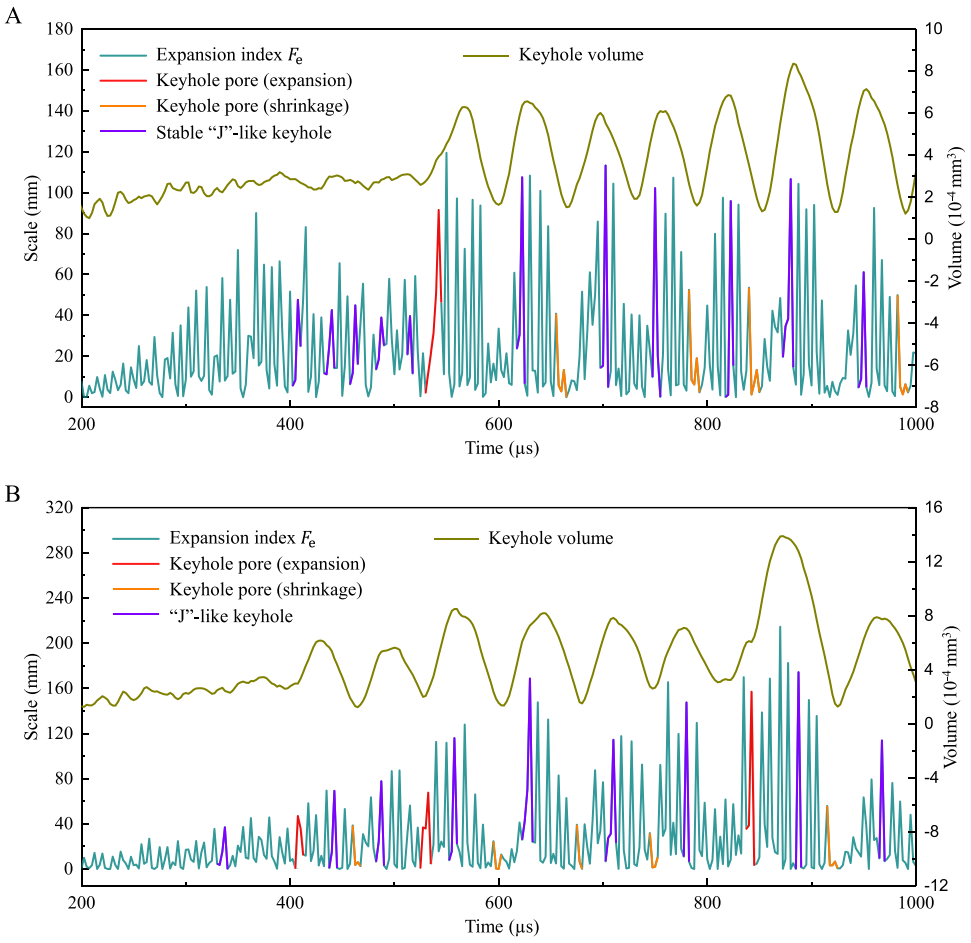

Fig. 11. The evolution of the expansion index F_e and the keyhole volume during the melting process. Only the portion of the keyhole with a depth greater than z_n is used to calculate the keyhole volume. (A) The laser power is 225 W and the scanning velocity is 50 cm/s. (B) The laser power is 225 W and the scanning velocity is 45 cm/s.

challenging to distinguish between the stable keyhole and the expansion-induced keyhole pore. Fig. 11 shows the regular occurrence of the formation and shrinkage of "J"-like keyholes during the laser melting process. One feasible way is to adopt optimization strategy in each cycle of the "J"-like keyhole formation. As demonstrated in Section 3.1.2, reducing the laser power during the initial stage of "J"-like keyhole formation can stabilize the keyhole and prevent the generation of keyhole pores.

During one cycle of "J"-like keyhole formation and shrinkage, the expansion index undergoes multiple sharp turning points, each characterized by a rapid increase followed by a rapid decrease. However, the change in keyhole volume only has a single turning point in one cycle. This difference indicates that the 2D parameter based on the central cross-section undergoes more significant fluctuations than the 3D parameter. In this study, all turning points are considered when implementing the optimization strategy, since it is difficult to determine such a turning point of the expansion index that corresponds to the initial stage in one cycle. More specifically, the optimization strategy is conducted when the deformation index in the last time interval is smaller than 0 ($(F_d)^{n-1} < 0$) and the increase of the expansion index is larger than a threshold ΔF ($(F_e)^n - (F_e)^{n-1} > \Delta F$). This criterion implies that the keyhole is shrinking during the last time interval and begins to expand in the current time interval, suggesting a possible initial stage of the "J"-like keyhole formation.

The threshold ΔF determines the frequency of applying the optimization strategy, and its selection should satisfy two requirements. First, the threshold ΔF should be larger than the secondary index increases (e.g., 600 μs in Fig. 11A) near the turning points between two cycles of the keyhole expansion and shrinkage. This ensures that the threshold filters out the small change in the expansion index caused by 2D fluctuations rather than 3D keyhole expansion and shrinkage. Second, the threshold ΔF should be smaller than the major index increases in one cycle of the keyhole expansion and shrinkage. This ensures that all possible initial stages of "J"-like keyhole formation will be considered in the optimization criterion. In experiments, it can be determined by conducting a standard experiment without optimization and analyzing the change in the expansion index during the laser melting process (e.g., Fig. 10).

3.3.2. *Optimization approach*

Compared to changing the laser direction, number of laser beams, and powder distribution, it is more cost-effective and practical to optimize the laser scanning strategy, including adjusting the laser power, scanning velocity, and scanning path [5,7,8]. The optimization of the scanning path is typically employed in a multi-track model [25–28], while this study only considers a single track for simplicity. Both laser power and scanning velocity directly affect the laser intensity, and there are two state-of-the-art adaptive laser power strategies [48,49] stabilizing the deep keyhole at the starting and turning points. Therefore, this study adopts adaptive laser power as an optimization approach throughout the entire scanning path. The primary objective of this work is to develop a proper laser strategy that utilizes adaptive laser power to stabilize keyhole fluctuation and prevent the formation of keyhole pores. By doing so, we aim to enhance both the manufacturing efficiency and the quality of the final product.

An adjusted laser power will be adopted when the optimization criterion is satisfied, i.e., $(F_d)^{n-1} < 0$ and $(F_e)^n - (F_e)^{n-1} > \Delta F$. Section 3.1.2 has shown the initial effectiveness of this optimization approach. Under the premise of stabilizing the keyhole and preventing the keyhole pore formation, it is preferable to use finer adjustment of laser power relative to the standard laser power, since it will not significantly impact manufacturing efficiency. A systematic study is required to determine appropriate adjustment of laser power with respect to the standard laser power.

4. Numerical results and discussion

In this section, we will examine the performance of the proposed optimization scheme in improving keyhole stability. Two parameters, namely the threshold for the increase in expansion index (ΔF) and the adjustment of laser power, will be comprehensively investigated. It should be noted that the adoption of the optimization scheme must meet three requirements: (1) Less impact on manufacturing efficiency: it is quantified by the keyhole depth in this study, serving as an indicator of the melting depth of a single track (which denotes the distance between the substrate surface to the bottom of the molten region). (2) Preventing expansion-induced keyhole pores. (3) Stabilizing keyhole fluctuations,

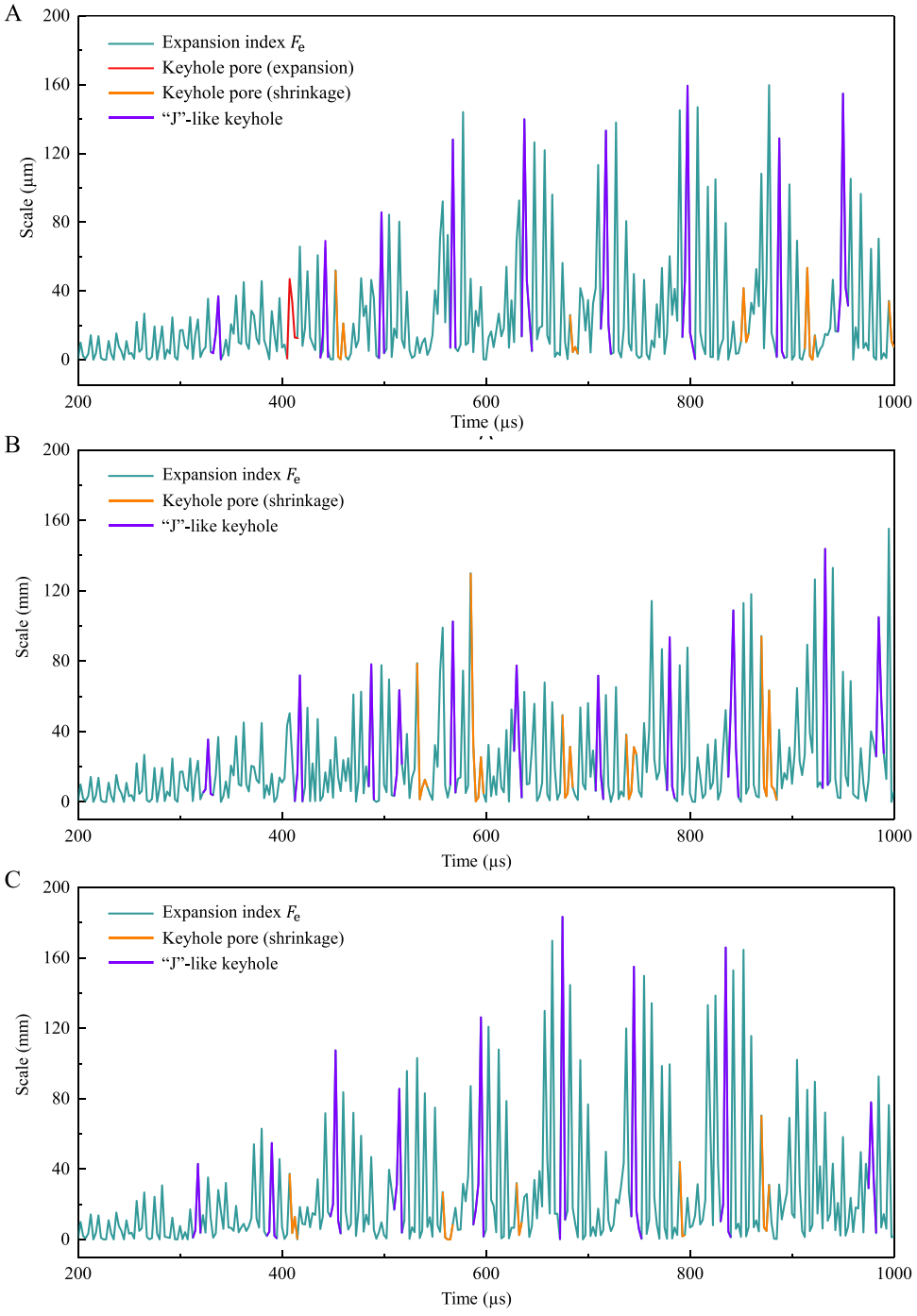

Fig. 12. The evolution of the expansion index F_e during the melting process, with three different thresholds for the increase in expansion index (ΔF) considered: 40 mm (A), 30 mm (B), and 20 mm (C), respectively.

particularly the expansion and shrinkage of the "J"-like keyhole, which is quantified by the variation of the keyhole volume, as shown in Fig. 11. The discussion focuses on the simulation results of the case with a scanning velocity of 45 cm/s in detail since it exhibits more expansion-induced keyhole pores, as demonstrated in Fig. 11.

4.1. Threshold for the increase in expansion index

Fig. 11B shows three representative cycles of expansion-induced keyhole pore formation, with a minimum increase in expansion index of 35.7 mm. Based on this minimum increase, three thresholds for the increase in expansion index are considered: 20 mm, 30 mm, and 40 mm. Given that this section focuses solely on the impact of the threshold for the increase in expansion index, the adjusted laser power is set to a constant value of 168.75 W, which is 75 % of the original laser power (225 W). The selection of the adjusted laser power will be discussed in Section 4.2. Fig. 12 and Fig. 13 present the evolution of the expansion index, adaptive laser power, keyhole volume, and keyhole central depth during the melting process, with three different thresholds considered.

The proposed optimization strategy enables to reduce keyhole fluctuations significantly, as evident by comparing the peak expansion index values in Fig. 11B and Fig. 12. Nonetheless, since the threshold of

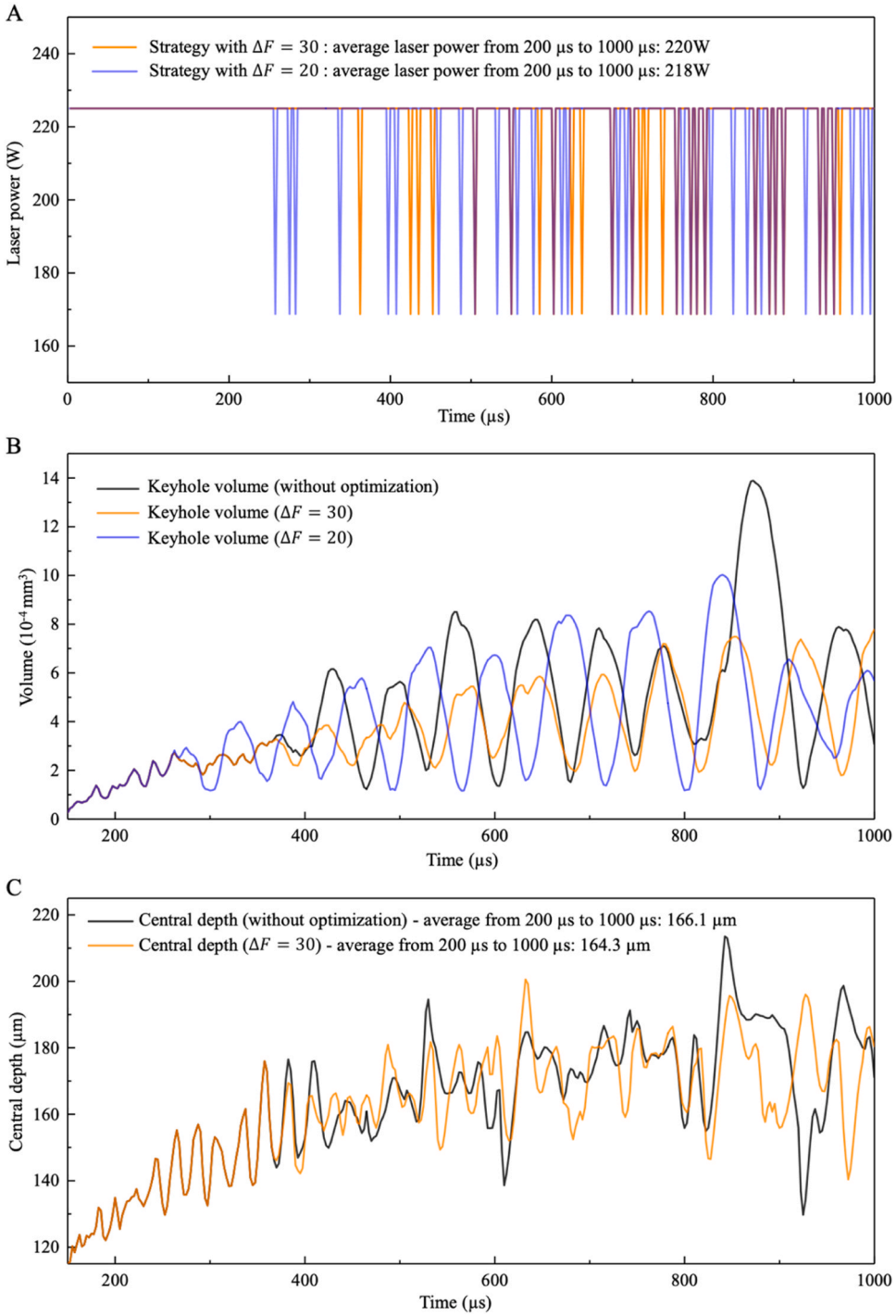

Fig. 13. The evolution of the laser power (A), keyhole volume (B), and keyhole central depth (C) during the melting process. Only the portion of the keyhole with a depth greater than 100 μm is used to calculate the volume and central depth of the keyhole.

40 mm is larger than the minimum increase in expansion index (35.7 mm), the optimization strategy cannot prevent the formation of all expansion-induced keyhole pores, as demonstrated in Fig. 12A. Using optimization strategies with thresholds of 20 mm and 30 mm can eradicate expansion-induced keyhole pores. It is important to emphasize that when the threshold for the increase in expansion index decreases, the optimization frequency increases (as depicted in Fig. 13A). This is because a lower threshold allows for the consideration of more deceptive fluctuations caused by the limited 2D information, thereby employing a weaker optimization criterion. Fig. 12 (B and C) and Fig. 13B demonstrate that keyhole fluctuations increase significantly when the optimization frequency exceeds a suitable value. Specifically, the case with a 20 mm threshold shows around a 42 % larger variation in the expansion index and a 75 % higher average amplitude of variation in the keyhole volume compared to the case with a threshold of 30 mm, even though the former uses a higher frequency. Therefore, employing a 30 mm threshold leads to reduced keyhole fluctuations.

To sum up, it is crucial to select an appropriate threshold for the increase in expansion index for the optimization. The threshold value can be determined based on the minimum increase in expansion index during the melting process without laser optimization. For instance, the threshold can be set slightly less than the minimum increase in expansion index. A parametric study can also be performed in experiments to determine a suitable threshold for the optimization. In this study, a threshold of 30 mm is deemed a suitable choice that satisfies the three requirements. The optimization strategy successfully prevents the formation of expansion-induced keyhole pores (Fig. 12B) and reduces keyhole fluctuations by approximately 30 % (Fig. 13B). Moreover, the average laser power and the average central depth of the keyhole in this case with the optimization strategy are 97.8 % and 98.7 %, respectively, of those without the optimization strategy, thereby ensuring manufacturing efficiency.

4.2. Adjustment of laser power

In this section, the effect of the adjustment of laser power on keyhole stability is studied by selecting three different ratios (0.6, 0.75, and 0.9) of the adjusted laser power to the standard laser power. The threshold for the increase in expansion index remains constant at 30 mm, based on the simulation results from the previous section.

All three cases involving the adjusted laser power (Fig. 12B and Fig. 14) exhibit a lower peak expansion index when compared to the case without laser optimization. However, except for the case using a laser power ratio of 0.75, the other two cases are unable to fully prevent the formation of expansion-induced keyhole pores, as demonstrated in Fig. 14. When the adjusted laser power is comparable to the original laser power, such as when the ratio is 0.9, the slight decrease in laser power is insufficient to effectively suppress keyhole expansion. The resulting peak expansion index (Fig. 14A) in this case is considerably greater than that observed in the case (Fig. 12B) where the laser power ratio is 0.75.

Conversely, when the adjusted laser power is extremely low (Fig. 14B), the keyhole fluctuations will once again be amplified, akin to the situation where the optimization frequency is excessively high, as discussed in Section 4.1. More specifically, Fig. 15A illustrates the evolution of the keyhole volume, which indicates that the magnitude of

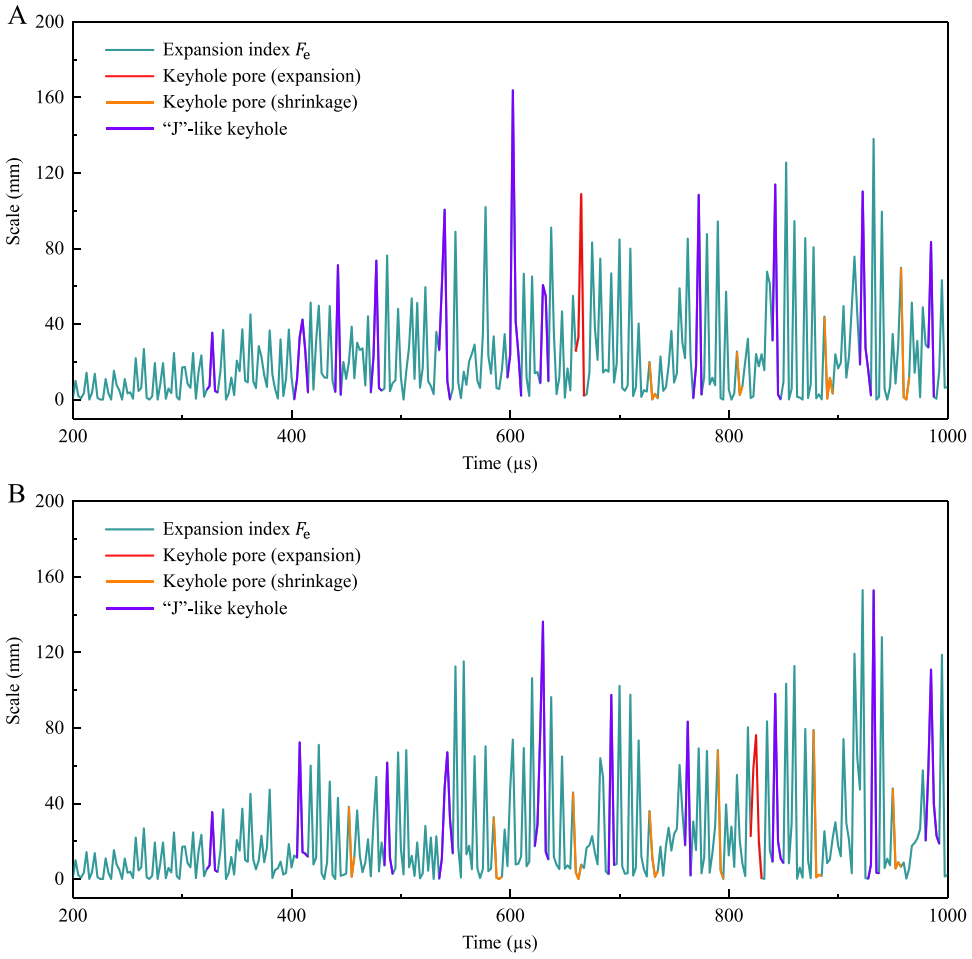

Fig. 14. The evolution of the expansion index F_e during the melting process, with two different ratios of the adjusted laser power to the standard laser power considered: 0.9 (A) and 0.6 (B), respectively. Note that, the case with a ratio of 0.75 is presented in Fig. 12B.

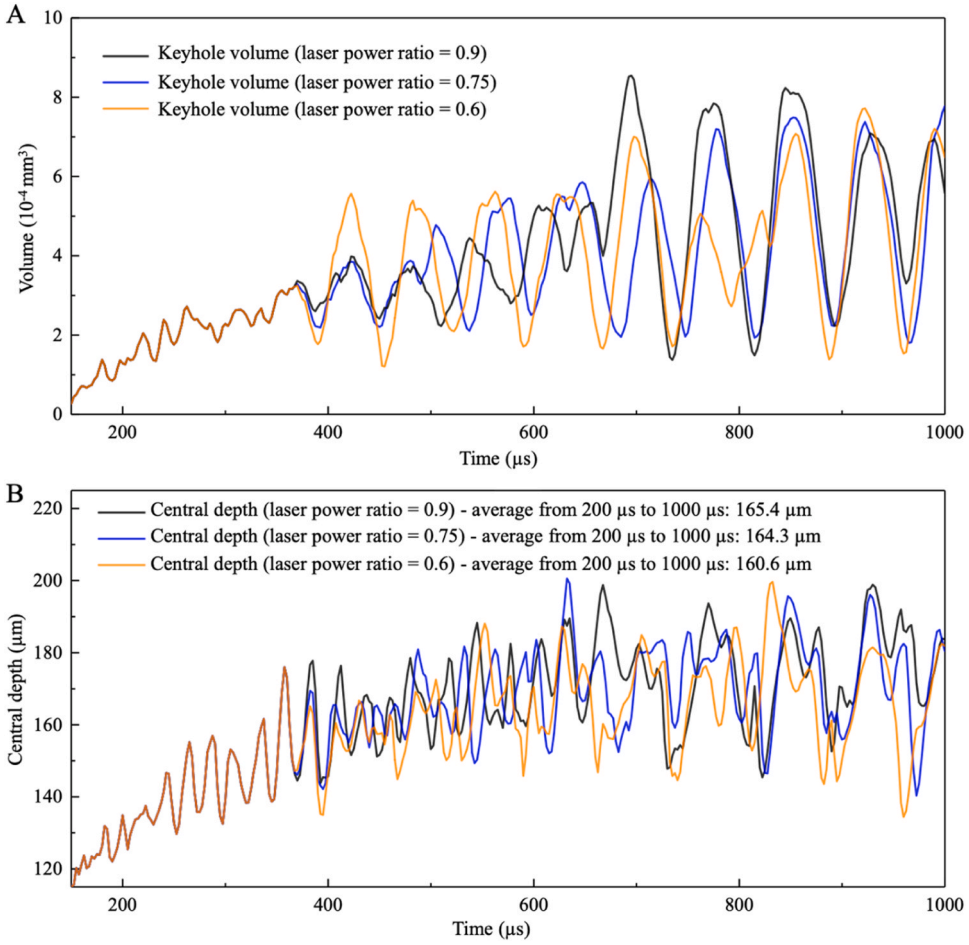

Fig. 15. The evolution of the keyhole volume (A), and keyhole central depth (B) during the melting process. Only the portion of the keyhole with a depth greater than 100 μm is used to calculate the volume and central depth of the keyhole.

fluctuations observed with a laser power ratio of 0.65 is significantly greater than those in the other two cases between 400 μs and 700 μs. Fig. 15B offers a further evidence that a decrease in adjusted laser power is associated with a greater reduction in both keyhole depth and the manufacturing efficiency. For instance, reducing the laser power ratio from 0.75 to 0.6 leads to a significant decrease (3.7 μm) in the central depth of the keyhole, compared to the decrease (1.1 μm) observed when the power ratio is reduced from 0.9 to 0.75. Note that, the original central depth of the keyhole is 166.1 μm, as depicted in Fig. 13B.

Such a significant decrease in the central depth of the keyhole arises due to the limitations of the 2D parameter, i.e., the expansion index, which fails to fully capture the 3D expansion and shrinkage process of the keyhole. During a complete cycle of keyhole expansion and shrinkage, the expansion index exhibits multiple significant fluctuations. Moreover, if the adjustment in laser power is dramatically large, multiple sudden decreases in laser power during a complete cycle of keyhole expansion and shrinkage can interrupt the continuous expansion of the keyhole and accelerate its shrinkage, further amplifying the fluctuations in the keyhole. This phenomenon explains why an expansion-induced keyhole pore can reoccur when the laser power ratio is set to 0.65. Hence, the selection of an appropriate laser adjustment should be determined through parametric studies using numerical simulations or experiments.

5. Conclusions

We propose an optimization strategy based on the mechanisms of keyhole instability. This strategy features a complete optimization framework consisting of optimization stages, optimization indices, and optimization criteria and approaches. We comprehensively examine the validity of this mechanism-based optimization strategy by high-fidelity, physics-based numerical simulations of keyhole formations. The simulation results demonstrate that the proposed optimization strategy can significantly reduce the keyhole fluctuations and prevent the formation of expansion-induced keyhole pores without sacrificing printing efficiency. Specifically, our new findings can be summarized as follows.

(1) During a compete keyhole pore-formation process, five stages can be identified: "J"-like keyhole formation, keyhole closure, keyhole pore collapse, keyhole pore splitting, and keyhole pore motion. Our numerical simulations indicate that decreasing the laser power at the onset of "J"-like keyhole formation appears to be an appropriate approach to enhance keyhole stability and prevent keyhole pore formation.
(2) Our numerical simulations capture three keyhole characteristics during a complete laser melting cycle: a stable "J"-like keyhole and two types of keyhole pores resulting from keyhole expansion and shrinkage. It is essential to prevent the expansion-induced keyhole pore for better manufacturing quality since it is the major contributor to keyhole porosity.
(3) To quantify the keyhole fluctuations during a complete laser melting process, we propose three adaptive indices: the deformation index, the absolute deformation index, and the expansion index. The optimization criterion is built on the three adaptive indices to determine the optimal time to adjust the laser power.

(4) Based on two parametric numerical studies on investigating the impact of the optimization criterion and laser power adjustment, it suggests that our proposed optimization strategy, with a moderate frequency and magnitude of laser power adjustment, can stabilize the keyhole and prevent the formation of keyhole pores while ensuring printing efficiency. It is recommended to determine future optimization criteria and laser power adjustment strategies through parametric studies using corroborative numerical simulations and experiments.

This study represents a crucial first step towards the development of an adaptive optimization strategy in L-PBF, utilizing a rigorous and physics-based computational approach. However, further improvements to the optimization strategy are required. First, the optimization criterion can be refined to improve its accuracy in predicting the formation of the "J"-like keyhole. The current criterion takes into account all potential "J"-like keyholes, given the limitations of the proposed 2D adaptive indices, resulting in a higher optimization frequency. Second, the optimization strategy utilizes a constant adjustment of the laser power, and the parametric study only examines limited cases with specific laser power and scanning velocity. Further optimization approaches could be developed to enhance keyhole stability and prevent the formation of keyhole pores through systematic studies under various manufacturing conditions. Third, this study solely employs numerical simulations to investigate the impact of the proposed optimization strategy. Various factors, such as monitoring delay and scanning resolution of monitoring equipment, can impact the optimization strategy in practical applications. Therefore, it is important to conduct systematic experiments to validate the findings of this study and adjust the optimization strategies if possible.

CRediT authorship contribution statement

Jidong Zhao: Writing – review & editing, Validation, Supervision, Project administration, Methodology, Investigation, Funding acquisition, Formal analysis, Conceptualization. **Shiwei Zhao:** Writing – review & editing, Visualization, Validation, Investigation, Formal analysis. **Tao Yu:** Writing – original draft, Visualization, Validation, Software, Resources, Methodology, Investigation, Formal analysis, Data curation, Conceptualization.

Declaration of Competing Interest

The authors declare that they have no known competing financial interests or personal relationships that could have appeared to influence the work reported in this paper.

Data availability

Data will be made available on request.

Acknowledgements

This study was supported by the National Natural Science Foundation of China (11972030, 52439001) and UGC Research Infrastructure Grant Scheme via Innovative Exploratory Grant # IEG22EG01. Tao Yu acknowledges the Hong Kong Ph.D. Fellowship support from the Research Grants Council of Hong Kong on his Ph.D. study.

Appendix A

Table A1 Physical parameters of Ti-6Al-4 V [6,32] and ambient gas [6,32] adopted for the simulations.

Parameter	Value and units	Parameter	Value and units
Room temperature	$T_0 = 300$ K	Solidus temperature	$T_s = 1878$ K
Liquidus temperature	$T_l = 1923$K	Boiling temperature	$T_{LV} = 3133$K
Molar mass	$M = 446.07$ g/mol	Convective heat transfer coefficient	h $= 19$ kg·s^{3}K
Viscosity of liquid Ti−6Al−4 V alloy	$\mu_l = 0.005$ Pa·s	Viscosity of solid Ti−6Al−4 V alloy	$\mu_l = 1.13$ Pa·s
Latent heat of fusion	$L_f = 2.88 \times 10^5$ m^2/s^2	Permeability coefficient	$K_c = 5.56 \times 10^6$ kg/(m^{3}s)
Latent heat of evaporation	$L_V = 9.7 \times 10^6$m^2/s^2	Constant to avoid division by zero	$C_k = 10^{-5}$
Surface tension coefficient at melt point	$\sigma_l = 1.68$ kg/s^2	Change rate of surface tension coefficient	$\frac{\partial \sigma}{\partial T} = -2.6 \times 10^{-4}$ kg/(s^{2}K)
Refractive index [53]	$e = 3.47$	Coefficient related to the electrical conductance [35]	$\varepsilon = 0.2$
Reflectivity at room temperature [54]	$f_{R0} = 0.95$	Reflectivity at liquidus temperature [54]	$f_{Rl} = 0.63$
Absorption coefficient at room temperature [1]	$\gamma_0 = 47.1$ μm^{-1}	Absorption coefficient at liquidus temperature [32,37,44,47]	$\gamma_0 = 0.192$ μm^{-1}
Gas density	$\rho_2 = 1.87$kg/m^3	Viscosity of gas	$\mu_2 = 2.5 \times 10^{-5}$Pa·s
Heat capacity of gas	$C_2 = 500$ J/(kg • K)	Thermal conductivity of gas	$k_2 = 0.021$ W/(m • K)

Table A2 Temperature-dependent thermal parameters of Ti-6Al-4 V [55] adopted for the simulations.

Material	Parameter and units	Value or equation
Ti−6Al−4 V	Density (kg/m^3)	$\rho_1 = \begin{cases} 4420 & T < 1268\ \text{K} \\ 4420 - 0.154(T - 298) & 1268\text{K} < T < 1923\ \text{K} \\ 3920 - 0.680(T - 1923) & T \geq 1923\ \text{K} \end{cases}$
	Heat capacity (J/(kg·K))	$C_1 = \begin{cases} 411.5 & T < 1268\ \text{K} \\ 411.5 + 0.2T + 5 \times 10^{-7} T^2 & 1268\text{K} < T < 1923\ \text{K} \\ 830 & T \geq 1923\ \text{K} \end{cases}$
	Thermal conductivity (W/(m·K))	$k_1 = \begin{cases} 19.0 & T < 1268\ \text{K} \\ -0.80 + 0.018T - 2 \times 10^{-6} T^2 & 1268\text{K} < T < 1923\ \text{K} \\ 33.4 & 1923\text{K} < T < 1973\ \text{K} \\ 34.6 & T \geq 1973\ \text{K} \end{cases}$

References

[1] C. Zhao, N.D. Parab, X. Li, K. Fezzaa, W. Tan, A.D. Rollett, T. Sun, Critical instability at moving keyhole tip generates porosity in laser melting, Science 370 (2020) 1080–1086.

[2] S. Beretta, S. Romano, A comparison of fatigue strength sensitivity to defects for materials manufactured by AM or traditional processes, Int. J. Fatigue 94 (2017) 178–191.

[3] H. Masuo, Y. Tanaka, S. Morokoshi, H. Yagura, T. Uchida, Y. Yamamoto, Y. Murakami, Influence of defects, surface roughness and HIP on the fatigue strength of Ti-6Al-4V manufactured by additive manufacturing, Int. J. Fatigue 117 (2018) 163–179.

[4] K.V. Yang, P. Rometsch, T. Jarvis, J. Rao, S. Cao, C. Davies, X. Wu, Porosity formation mechanisms and fatigue response in Al-Si-Mg alloys made by selective laser melting, Mater. Sci. Eng. A 712 (2018) 166–174.

[5] R. Lin, H.-p Wang, F. Lu, J. Solomon, B.E. Carlson, Numerical study of keyhole dynamics and keyhole-induced porosity formation in remote laser welding of Al alloys, Int. J. Heat. Mass Transf. 108 (2017) 244–256.

[6] L. Wang, Y. Zhang, H.Y. Chia, W. Yan, Mechanism of keyhole pore formation in metal additive manufacturing, npj Comput. Mater. 8 (2022) 1–11.

[7] N.T. Aboulkhair, N.M. Everitt, I. Ashcroft, C. Tuck, Reducing porosity in AlSi10Mg parts processed by selective laser melting, Addit. Manuf. 1 (2014) 77–86.

[8] M. Ma, Z. Wang, M. Gao, X. Zeng, Layer thickness dependence of performance in high-power selective laser melting of 1Cr18Ni9Ti stainless steel, J. Mater. Process. Technol. 215 (2015) 142–150.

[9] A.A. Martin, N.P. Calta, S.A. Khairallah, J. Wang, P.J. Depond, A.Y. Fong, V. Thampy, G.M. Guss, A.M. Kiss, K.H. Stone, Dynamics of pore formation during laser powder bed fusion additive manufacturing, Nat. Commun. 10 (2019) 1987.

[10] S.A. Khairallah, A.A. Martin, J.R.I. Lee, G. Guss, N.P. Calta, J.A. Hammons, M. H. Nielsen, K. Chaput, E. Schwalbach, M.N. Shah, M.G. Chapman, T.M. Willey, A. M. Rubenchik, A.T. Anderson, Y.M. Wang, M.J. Matthews, W.E. King, Controlling interdependent meso-nanosecond dynamics and defect generation in metal 3D printing, Science 368 (2020) 660–665.

[11] Z. Ren, L. Gao, S.J. Clark, K. Fezzaa, P. Shevchenko, A. Choi, W. Everhart, A. D. Rollett, L. Chen, T. Sun, Machine learning–aided real-time detection of keyhole pore generation in laser powder bed fusion, Science 379 (2023) 89–94.

[12] D. Bourell, B. Stucker, A. Spierings, N. Herres, G. Levy, Influence of the particle size distribution on surface quality and mechanical properties in AM steel parts, Rapid Prototyp. J. (2011).

[13] J. Metelkova, Y. Kinds, K. Kempen, C. de Formanoir, A. Witvrouw, B. Van Hooreweder, On the influence of laser defocusing in Selective Laser Melting of 316L, Addit. Manuf. 23 (2018) 161–169.

[14] C. Qiu, C. Panwisawas, M. Ward, H.C. Basoalto, J.W. Brooks, M.M. Attallah, On the role of melt flow into the surface structure and porosity development during selective laser melting, Acta Mater. 96 (2015) 72–79.

[15] R. Li, J. Liu, Y. Shi, L. Wang, W. Jiang, Balling behavior of stainless steel and nickel powder during selective laser melting process, Int. J. Adv. Manuf. Technol. 59 (2012) 1025–1035.

[16] H. Ali, L. Ma, H. Ghadbeigi, K. Mumtaz, In-situ residual stress reduction, martensitic decomposition and mechanical properties enhancement through high temperature powder bed pre-heating of Selective Laser Melted Ti6Al4V, Mater. Sci. Eng.:A 695 (2017) 211–220.

[17] Y. Li, D. Gu, Parametric analysis of thermal behavior during selective laser melting additive manufacturing of aluminum alloy powder, Mater. Des. 63 (2014) 856–867.

[18] H.Y. Jung, S.J. Choi, K.G. Prashanth, M. Stoica, S. Scudino, S. Yi, U. Kühn, D. H. Kim, K.B. Kim, J. Eckert, Fabrication of Fe-based bulk metallic glass by selective laser melting: A parameter study, Mater. Des. 86 (2015) 703–708.

[19] A. Okunkova, M. Volosova, P. Peretyagin, Y. Vladimirov, I. Zhirnov, A.V. Gusarov, Experimental approbation of selective laser melting of powders by the use of non-Gaussian power density distributions, Phys. Procedia 56 (2014) 48–57.

[20] P. Kumar, J. Farah, J. Akram, C. Teng, J. Ginn, M. Misra, Influence of laser processing parameters on porosity in Inconel 718 during additive manufacturing, Int. J. Adv. Manuf. Technol. 103 (2019) 1497–1507.

[21] D. Grange, A. Queva, G. Guillemot, M. Bellet, J.-D. Bartout, C. Colin, Effect of processing parameters during the laser beam melting of Inconel 738: comparison between simulated and experimental melt pool shape, J. Mater. Process. Technol. 289 (2021) 116897.

[22] I. Yadroitsev, L. Thivillon, P. Bertrand, I. Smurov, Strategy of manufacturing components with designed internal structure by selective laser melting of metallic powder, Appl. Surf. Sci. 254 (2007) 980–983.

[23] Y. Zhou, W. Li, L. Zhang, S. Zhou, X. Jia, D. Wang, M. Yan, Selective laser melting of Ti–22Al–25Nb intermetallic: significant effects of hatch distance on microstructural features and mechanical properties, J. Mater. Process. Technol. 276 (2020) 116398.

[24] D. Grange, J.-D. Bartout, B. Macquaire, C. Colin, Processing a non-weldable nickel-base superalloy by selective laser melting: role of the shape and size of the melt pools on solidification cracking, Materialia 12 (2020) 100686.

[25] H. Shipley, D. McDonnell, M. Culleton, R. Coull, R. Lupoi, G. O'Donnell, D. Trimble, Optimisation of process parameters to address fundamental challenges during selective laser melting of Ti-6Al-4V: a review, Int. J. Mach. Tools Manuf. 128 (2018) 1–20.

[26] C. Qiu, N.J. Adkins, M.M. Attallah, Microstructure and tensile properties of selectively laser-melted and of HIPed laser-melted Ti–6Al–4V, Mater. Sci. Eng. A 578 (2013) 230–239.

[27] M.F. Zaeh, G. Branner, Investigations on residual stresses and deformations in selective laser melting, Prod. Eng. 4 (2010) 35–45.

[28] Q. Chen, J. Liu, X. Liang, A.C. To, A level-set based continuous scanning path optimization method for reducing residual stress and deformation in metal additive manufacturing, Comput. Methods Appl. Mech. Eng. 360 (2020) 112719.

[29] Z. Wang, M. Liu, Dimensionless analysis on selective laser melting to predict porosity and track morphology, J. Mater. Process. Technol. 273 (2019) 116238.

[30] M. Rombouts, J.-P. Kruth, L. Froyen, P. Mercelis, Fundamentals of selective laser melting of alloyed steel powders, CIRP Ann. 55 (2006) 187–192.

[31] T. Yu, J. Zhao, Quantifying the mechanisms of keyhole pore evolutions and the role of metal-vapor condensation in laser powder bed fusion, Addit. Manuf. (2023) 103642.

[32] T. Yu, J. Zhao, Semi-coupled resolved CFD–DEM simulation of powder-based selective laser melting for additive manufacturing, Comput. Methods Appl. Mech. Eng. 377 (2021) 113707.

[33] T. Yu, J. Zhao, Quantitative simulation of selective laser melting of metals enabled by new high-fidelity multiphase, multiphysics computational tool, Comput. Methods Appl. Mech. Eng. 399 (2022) 115422.

[34] R. Cunningham, C. Zhao, N. Parab, C. Kantzos, J. Pauza, K. Fezzaa, T. Sun, A. D. Rollett, Keyhole threshold and morphology in laser melting revealed by ultrahigh-speed x-ray imaging, Science 363 (2019) 849–852.

[35] M. Bayat, A. Thanki, S. Mohanty, A. Witvrouw, S. Yang, J. Thorborg, N.S. Tiedje, J. H. Hattel, Keyhole-induced porosities in Laser-based Powder Bed Fusion (L-PBF) of Ti6Al4V: high-fidelity modelling and experimental validation, Addit. Manuf. 30 (2019) 100835.

[36] C. Tang, J.L. Tan, C.H. Wong, A numerical investigation on the physical mechanisms of single track defects in selective laser melting, Int. J. Heat. Mass Transf. 126 (2018) 957–968.

[37] Z. Wang, W. Yan, W.K. Liu, M. Liu, Powder-scale multi-physics modeling of multi-layer multi-track selective laser melting with sharp interface capturing method, Comput. Mech. 63 (2019) 649–661.

[38] C. Panwisawas, C. Qiu, Y. Sovani, J. Brooks, M. Attallah, H. Basoalto, On the role of thermal fluid dynamics into the evolution of porosity during selective laser melting, Scr. Mater. 105 (2015) 14–17.

[39] L. Wang, Y. Zhang, W. Yan, Evaporation model for keyhole dynamics during additive manufacturing of metal, Phys. Rev. Appl. 14 (2020) 064039.

[40] M. Knudsen, Die maximale verdampfungsgeschwindigkeit des quecksilbers, Ann. der Phys. 352 (1915) 697–708.

[41] A. Badillo, Quantitative phase-field modeling for boiling phenomena, Phys. Rev. E 86 (2012) 041603.

[42] A.A. Badillo, in: ASME International Mechanical Engineering Congress and Exposition, American Society of Mechanical Engineers, 2013.

[43] R. Szijártó, A. Badillo, B. Ničeno, H.-M. Prasser, Condensation models for the water–steam interface and the volume of fluid method, Int. J. Multiph. Flow. 93 (2017) 63–70.

[44] J. Tan, C. Tang, C. Wong, Study and modeling of melt pool evolution in selective laser melting process of SS316L, MRS Commun. 8 (2018) 1178–1183.

[45] Z.S. Saldi, Marangoni Driven Free Surface Flows in Liquid Weld Pools (2012).

[46] J.U. Brackbill, D.B. Kothe, C. Zemach, A continuum method for modeling surface tension, J. Comput. Phys. 100 (1992) 335–354.

[47] C. Panwisawas, C. Qiu, M.J. Anderson, Y. Sovani, R.P. Turner, M.M. Attallah, J. W. Brooks, H.C. Basoalto, Mesoscale modelling of selective laser melting: thermal fluid dynamics and microstructural evolution, Comput. Mater. Sci. 126 (2017) 479–490.

[48] S.A. Khairallah, A.A. Martin, J.R. Lee, G. Guss, N.P. Calta, J.A. Hammons, M. H. Nielsen, K. Chaput, E. Schwalbach, M.N. Shah, Controlling interdependent meso-nanosecond dynamics and defect generation in metal 3D printing, Science 368 (2020) 660–665.

[49] A.A. Martin, N.P. Calta, S.A. Khairallah, J. Wang, P.J. Depond, A.Y. Fong, V. Thampy, G.M. Guss, A.M. Kiss, K.H. Stone, Dynamics of pore formation during laser powder bed fusion additive manufacturing, Nat. Commun. 10 (2019) 1–10.

[50] L. Caprio, A.G. Demir, B. Previtali, Observing molten pool surface oscillations during keyhole processing in laser powder bed fusion as a novel method to estimate the penetration depth, Addit. Manuf. 36 (2020) 101470.

[51] B.J. Simonds, J. Sowards, J. Hadler, E. Pfeif, B. Wilthan, J. Tanner, C. Harris, P. Williams, J. Lehman, Time-resolved absorptance and melt pool dynamics during intense laser irradiation of a metal, Phys. Rev. Appl. 10 (2018) 044061.

[52] Y. Huang, T.G. Fleming, S.J. Clark, S. Marussi, K. Fezzaa, J. Thiyagalingam, C.L. A. Leung, P.D. Lee, Keyhole fluctuation and pore formation mechanisms during laser powder bed fusion additive manufacturing, Nat. Commun. 13 (2022) 1–11.

[53] X. Li, C. Zhao, T. Sun, W. Tan, Revealing transient powder-gas interaction in laser powder bed fusion process through multi-physics modeling and high-speed synchrotron x-ray imaging, Addit. Manuf. 35 (2020) 101362.

[54] M.S. William, M. Jyotirmoy, Laser Material Processing, 3, Steen springer-Verlag, London, Berlin, Heidelberg, 2010, p. 408.

[55] J.J. Valencia, P.N. Quested, Thermophysical Properties, (2013).